JOURNAL OF SPACECRAFT AND ROCKETS
Vol. 42, No. 3, May–June 2005

# Cold-Flow Testing of Subscale Model Exhaust System for Space-Based Laser

I. S. Bautista,* S. E. Bergren,† and M. E. Franke‡
*Air Force Institute of Technology, Wright–Patterson Air Force Base, Ohio 45433*

**High-speed airflow through stacked rings of nozzles and an exhaust manifold is described. The rings and exhaust manifold are part of a scale model of one quadrant of the conceptual Space-Based Laser Integrated Flight Experiment chemical laser. This model consisted of a nozzle array, centerbody, and supersonic diffuser. A transition structure mated the test section to a blowdown/vacuum system. Rapid data acquisition and schlieren photography indicated that quasi-steady supersonic flow lasted for approximately 10 s from startup until the vacuum system pressure increased. During the test, a well-defined oblique shock wave was attached to the leading edge of the centerbody, where the flow reached a Mach number of 2.8.**

## Nomenclature

$A$ = cross-sectional area
$a$ = speed of sound
$M$ = Mach number
$\dot{m}$ = mass-flow rate
$o$ = stagnation
$p$ = pressure
$R$ = specific gas constant
$T$ = temperature
$t$ = time
$\gamma$ = ratio of specific heats

## Introduction

LASERS have been tested as an effective weapon against missiles since 1973. During that time, the mid-infrared advanced chemical laser was developed and first tested against tactical missiles and drone aircraft. This laser weapon concept is currently being pursued with the airborne laser program, which fits a chemical oxygen–iodine laser into a Boeing 747 aircraft. Its objective is to destroy ballistic missiles during the boost phase of their flight.[1]

The Space-Based Laser Integrated Flight Experiment (SBL IFX) shared in this concept by investigating the possibility of placing chemical lasers (CLs) in space rather than on aircraft. The SBL IFX was to prove the technology necessary to employ megawatt-class CLs to destroy ballistic missiles in their boost phase of flight.[2,3] The U. S. government contract was with three partners, the Boeing Co., Lockheed Martin Corp., and TRW, Inc., where TRW would supply the laser.

The power generated in the SBL IFX is a result of an exothermic reaction of hydrogen and dissociated fluorine. An array of nozzles accelerates the fluorine molecules supersonically. Molecular hydrogen is injected into the supersonic expansion at the nozzle exit to enable good mixing and efficient reaction with the fluorine to produce the vibrationally inverted HF molecules required for lasing. The HF is formed in a low-pressure, low-temperature, high-speed flow that reduces the HF deactivation rates and stretches the reaction zone.[4]

The flow structure in the nozzles, the lasing cavity, and the exhaust manifold is critical to the laser performance. The beam quality is strongly dependent on the homogeneity of the lasing medium. Shock waves and boundary-layer separation in the lasing cavity are sources of beam distortion.[2,3]

TRW was responsible for the laser power-generation portion of the SBL IFX. This segment of the SBL IFX is where the population inversion occurs, causing the initial lasing. TRW designed a nozzle array and diffuser that theoretically will create a laser in the megawatt class. Two-dimensional computational fluid dynamics (CFD) by TRW has yielded preliminary results for the flow characteristics in the proposed design.[2,3] The internal fluid flow downstream of a single quadrant of the nozzle array associated with this high-power chemical laser is the focus of this study.

A cross-sectional view of a single quadrant of the SBL IFX is shown in Fig. 1. The nozzle array, center body, diffuser, and lasing cavity are together known as the exhaust manifold assembly (EMA).

This research effort had two major objectives. The first objective was to remodel the previous test facility so that it would be capable of investigating flow conditions in a simulated laser nozzle assembly and lasing cavity by using cold flow. The second objective was to examine the flow properties of the scaled nozzle/diffuser system by using time-based pressure measurements and schlieren photography.

The previous test facility[5,6] was modified and used in this study to test a scale model of a 90-deg segment of the proposed TRW design. Primarily, the transition structure that mated the model to the existing blowdown wind tunnel was redesigned. The objectives were accomplished by using rapid data acquisition for static pressures at various locations and improved viewing areas for schlieren photography for flow visualization, including shock waves and areas of separation.

## Test Section

The test section was scaled appropriately from the conceptual SBL IFX to fit the confines of the Air Force Institute of Technology test facility. This scaled model allowed the test section to be large enough to reduce viscous effects from walls, yet small enough to fit within the testing facility.

### Nozzle Array

Figure 2 is a computer-generated model of the nozzle array with hardware attachment points. There are a few notable differences between the scaled nozzle array and the SBL IFX. Hydrogen was not injected into the flow as it exited the nozzles during testing, and cold flow (air) was used in the test rather than the hydrogen and flourine used in the real design. Also, for manufacturing purposes, the nozzle walls were straight rather than contoured as with the

Presented as Paper 2003-3754 at the AIAA 34th Plasmadynamics and Lasers Conference, Orlando, FL, 23–26 June 2003; received 6 August 2003; revision received 27 February 2004; accepted for publication 2 June 2004. 

*Captain, U.S. Air Force; currently System Integration IPT Lead, Munitions Directorate, Eglin Air Force Base, FL 32542.
†Captain, U.S. Air Force; currently Flight Commander, 23rd Training Squadron, Maxwell Air Force Base, AL 36112.
‡Professor. Associate Fellow AIAA.

**Table 1 Nozzle dimensions[5]**

| Designation | Nomenclature | Dimension |
|---|---|---|
| a | Base | 4.6 mm |
| b | Exit width | 1.98 mm |
| c | Throat width | 1 mm |
| d | Half-angle | 15 deg |

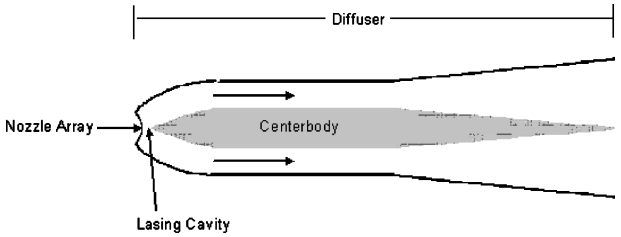


**Fig. 1 Cross-sectional view of one quadrant of the SBL IFX.**

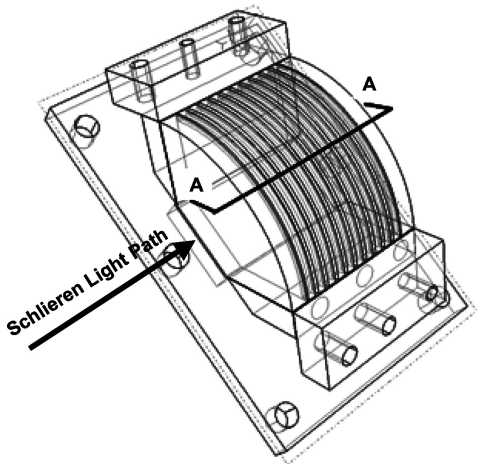


**Fig. 2 Nozzle array model.[5]**

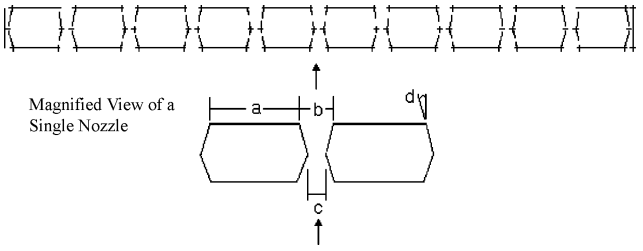


**Fig. 3 Cross section *A-A* (Fig. 2) of nozzle array.[5]**

real nozzle design. However, the main objective when designing the scaled nozzles was not to achieve similar fluid properties, but rather to produce similar Mach numbers at the exit plane. The nominal exit Mach number of the nozzle array is approximately 2.2. This was chosen to match the real design. A cross-sectional view of the model nozzle array is shown in Fig. 3 and a summary of the measurements is shown in Table 1. The schlieren optical path is also shown in Fig. 2 (see Ref. 5).

The losses due to the walls of the nozzles were needed in designing the exit velocity of the nozzle array. It was determined that the Mach number for straight walls was approximately 15% less than the Mach number for contoured walls designed for isentropic expansion. Figure 4 is a photograph of the constructed model nozzle array inside the test section.[5] Schlieren photography was used to observe the flow downstream of the nozzles with the light-beam path as shown in Fig. 2.

A straight nozzle array, consisting of four separate nozzles, was fabricated and attached to the stilling chamber as shown in Fig. 5. Shock interactions between the individual nozzles could now be seen

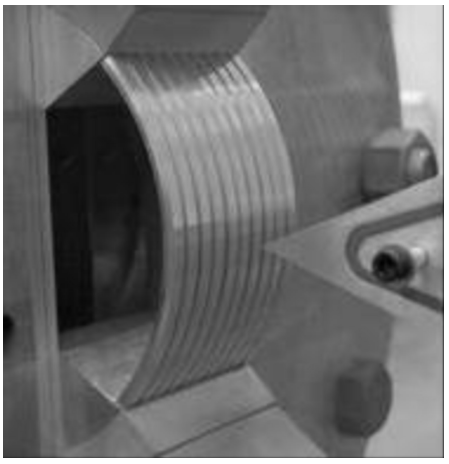

**Fig. 4 Photograph of nozzle array and leading edge of centerbody.**

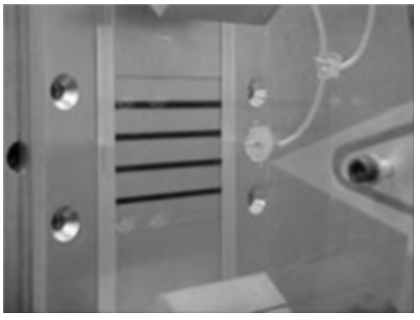

**Fig. 5 Straight nozzle array.**

with the schlieren light path as shown in Fig. 2. The dimensions were two times larger than the curved nozzle array to give a larger image of the shock interactions. The schlieren light path was the same as shown in Fig. 2, except that here, the light path was along the span of the nozzles rather than across the nozzles.

### Exhaust Manifold Assembly

The EMA is a diffuser designed to control the fluid flow. The EMA contains both the nozzle array and a centerbody positioned in the center of the EMA. The leading edge of the centerbody is 3.05 cm downstream of the nozzle array at the closest distance from the nozzle rings. The contour for the top and bottom walls of the diffuser was designed and provided by TRW. These symmetrical top and bottom pieces were designed with one contoured and two straight sections to direct the radial flow exiting the nozzles to a horizontal flow while minimizing losses. The three segments can be replaced by different geometries to further investigate the optimal design for redirecting the flow. This aids in the design goal of modularity. After the scaling, the diffuser was 1.41 m long with a height that ranged from 33.3 cm at the entrance to 47 cm at the exit plane. The majority of the sidewalls for the EMA were constructed from aluminum, but the first 76 cm was made of optical-grade Plexiglas to observe the flow characteristics within the cavity downstream of the nozzle array and around the centerbody. This was one of the main changes from the sidewalls of the test section before reconstruction. Initially, the Plexiglas extended only 30.5 cm downstream and allowed flow visualization only of the optical cavity and around the leading edge of the centerbody.[5,6] With the extension of the Plexiglas, flow around the midsection of the centerbody could be observed in addition to the cavity and leading edge.

### Transition Structure

The design of the transition section was critical in directing flow from the subscale EMA to the vacuum system, but still accurately modeling the SBL IFX. Initially, the transition structure connected the exit plane of the diffuser to the vacuum system by using

a rectangular section measuring 76.2 cm in length, which decreased in height until it mated with the vacuum line. This caused the flow to choke at the transition exit and shortened the test run time dramatically.[5,6]

The new transition structure mates to the diffuser exit in the same way that the previous one did. The only difference, however, is that instead of staying completely rectangular in shape, this new structure conforms to a circular shape as it meets the vacuum line. This relieved the choked flow condition at the exit. Figs. 6 and 7 show photographs of the previous and remodeled transition structures.

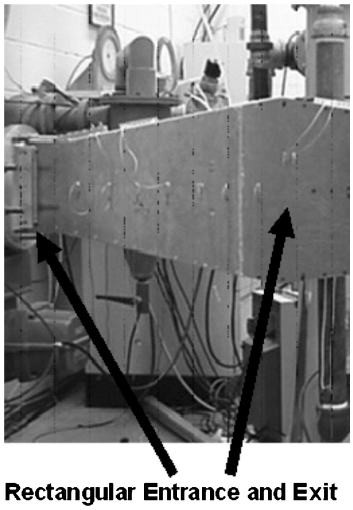


**Fig. 6 Previous transition structure photograph.[5]**

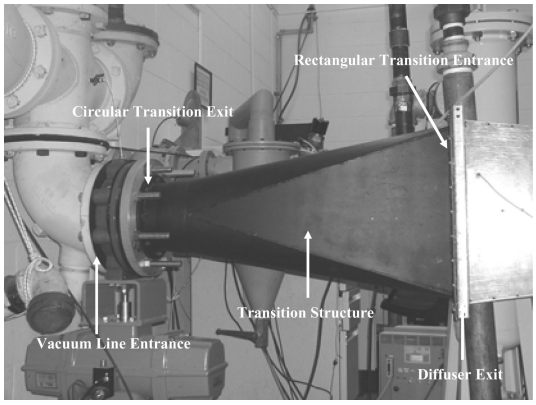


**Fig. 7 Remodeled-transition-structure photograph.**

## Wind-Tunnel System

The wind-tunnel system used for this research consisted of a blowdown/vacuum combination, which delivered a mass flow of almost 0.5 kg/s. This wind-tunnel system had three subsystems: a compressed air system, a pressure-regulating system, and a vacuum system. A schematic of the entire circuit can be seen in Fig. 8.

### Compressed Air System

The flow starts from the two Ingersoll–Rand SSR HXP 50 SE air compressors. These compressors provided compressed air at up to 150 psi. After exiting the compressors, the air was filtered through two Ingersoll–Rand air dryers where moisture and unwanted air particles were removed. From there, a 22.7-$m^3$ (6000-gal) supply tank was filled and pressurized to the same pressure as the discharged compressor air.

### Pressure Regulation System

After the supply tank was filled and pressurized, a diaphragm-type pressure regulator was used to reduce the supply air to a pressure of 0.62 MPa (90 psi). A 2-in., air-loaded pressure-reducing valve then reduced the pressure even further to a value set using an analog gauge controlled by the operator. The reducing valve was able to establish a set pressure reduction by balancing the pressure difference across its diaphragm. The reducing pressure range was 83 kPa–0.9 MPa (12–133 psi). A 12-in.-diam stilling chamber acted as a reservoir immediately upstream of the nozzles and test section. This provided a reservoir of air at near stagnation conditions. A flow straightener was built into the downstream end of the stilling chamber to provide straight flow through the nozzles. A shutoff valve allowed the supply air to enter the test section with a switch controlled by the operator.

### Vacuum System

A 22.7-$m^3$ (6000-gal) vacuum tank was evacuated by a Stokes Model 412 MBX two-stage pumping unit to provide the vacuum required to operate the wind tunnel. The pumping unit consisted of a Stokes Model 412-11 Microvac pump and a first-stage blower driven by 10- and 320-hp motors, respectively. When the shut-off valve was switched on, compressed air passed through the test section to the vacuum tank at the end. This would allow the wind tunnel to operate for approximately 30 s for each run. Between runs, the pumping unit could evacuate the vacuum system within 20 min to reach a minimum pressure of approximately 3 torr (0.06 psia).

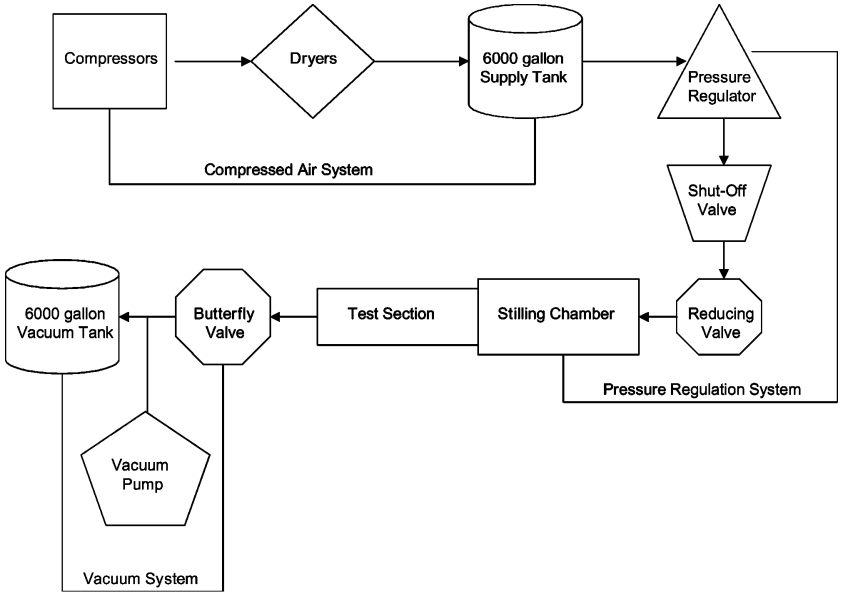


**Fig. 8 Wind-tunnel system.**

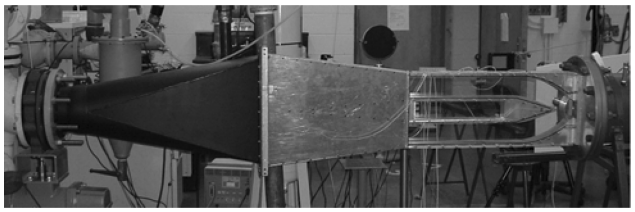

**Fig. 9 Fully assembled subscale model apparatus.**

A slow-action pneumatic butterfly valve was positioned where the vacuum line and the downstream end of the transition section mated together. When the valve was switched to the open position, the test section was subjected to the vacuum. The length of the vacuum line from the test section to the vacuum tank was 22.25 m (73 ft) with a diameter of 19.05 cm (7.5 in.). Six 90-deg and two 45-deg elbows existed in the line.

The fully assembled model was completed by mating the test section to the existing wind-tunnel system using the new remodeled transition structure. A photograph of the fully assembled apparatus is shown in Fig. 9.

## Data Collection

Schlieren photographs and pressure measurements were taken throughout the length of the test section to accomplish the objectives of this research. The need to capture a large number of data points required the use of a rapid-data-acquisition system. This provided for static pressure readings at various locations to supplement the schlieren photographs.

### Pressure Transducers

A total of seven Endevco Model 8530C-50 miniature high-sensitivity piezoresistive pressure transducers (PTs) were used to collect static-pressure measurements at the various locations at a frequency of 40 kHz. The seven transducers had a pressure range of 0–50 psia. The excitation voltage was 10 Vdc.

### Data-Acquisition System

The Nicolet MultiPro 120 was the data-acquisition system (DAS) used for this research. This multichannel data-acquisition unit was controlled by a 386 class computer running Microsoft Windows. The basics of the system included a seven-slot tower acquisition unit and four MP120 channel cards consisting of four channels each. The system was set to sample at a rate of 100 Hz or approximately one reading every 10 ms. All readings from the pressure transducers were fed to Endevco Model 4428A signal conditioners, which filtered and amplified the signals for the DAS. These signals were then digitized by the channel cards. The system controller would then read the digitized data via a general-purpose interface bus for display on the computer screen using Microsoft Windows.

### Schlieren Optical System

Images of density gradients were obtained in the cavity and parts of the diffuser by using a schlieren optical system. The light source was a cylindrical filament that was directed at a mirror 80 in. away. A vertical knife edge cut the light to see density gradients in the horizontal direction. The viewing screen was a large piece of white posterboard that allowed clear images of the test section. A high-resolution Photron FASTCAM-X 1280PCI digital camera was used to capture the video from the viewing screen at a rate of 60 frames per second.

### Pressure-Transducer Configuration

The pressure-transducer locations used with the curved nozzle array (Fig. 4) are indicated in the sketch in Fig. 10. In addition, transducers were placed in the stilling chamber and downstream of the test section in the facility vacuum line. For the straight nozzle array, data were collected by a pressure transducer 0.25 in. downstream of the nozzle exit plane. Table 2 provides cross-sectional flow areas corresponding to the locations of transducers 1–5. The areas listed for PT2 to PT4 are for only the upper half of the test section. These reference areas were used because the flow was assumed to be symmetric about the centerbody.

**Table 2 Cross-sectional areas for PT configuration**

| Pressure transducer | Cross-sectional area, $cm^2$ ($in.^2$) |
|---|---|
| 1 | $A_1 = 89.3\ (13.8)$ |
| 2 | $A_2 = 58.5\ (9.1)$ |
| 3 | $A_3 = 59.5\ (9.2)$ |
| 4 | $A_4 = 72.9\ (11.3)$ |
| 5 | $A_5 = 150.3\ (23.3)$ |

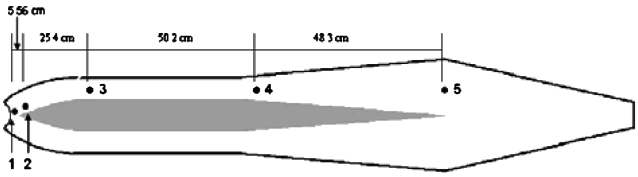


**Fig. 10 Pressure-transducer locations for curved array.**

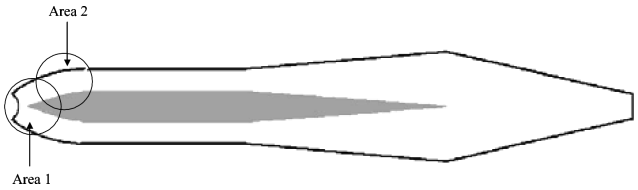


**Fig. 11 Viewing areas 1 and 2.**

Two viewing areas were used to capture schlieren images in the test section. Figure 11 illustrates the viewing areas for both the curved and straight nozzle arrays.

## Experimental Procedure

A portable pneumatic tester was used to calibrate the pressure transducers at two separate pressure values. All transducers were recalibrated approximately every three days to ensure accuracy. The uncertainty for a single pressure measurement was ±0.3 psi. This resulted from bias and precision error in both the pressure transducer and the signal conditioner. This uncertainty in pressure also affected the calculations of Mach number and mass flow rate.[5]

### Wind-Tunnel Operation

Initially all air valves were closed, and the camera capturing the schlieren images was switched to record. First, the butterfly valve was opened to allow the vacuum to pull through the test section, stilling chamber (reservoir), and plumbing all the way to the supply valve. This would then trigger the DAS. The system was allowed to settle for 1–2 s. Then the air shutoff valve was opened to release the compressed air through the system. The valve remained open until supersonic flow was no longer produced from the nozzles. The lack of gradients in the schlieren images determined this. The air shutoff valve was then closed, followed by the butterfly valve. The DAS stopped collecting data automatically after a 30-s time lapse. The results were immediately displayed graphically on a computer monitor.

### Cold-Flow Analysis

The mass flow of a thermally and calorically perfect gas through a choked supersonic nozzle is given in terms of stagnation properties by

$$\dot{m} = \left(p_0 A^* \Big/ \sqrt{T_0}\right)\sqrt{(\gamma/R)[2/(\gamma+1)]^{(\gamma+1)/(\gamma-1)}} \qquad (1)$$

where the Mach number at the throat is known to be unity.[7]

Assuming steady flow, conservation of mass can be used to find the instantaneous Mach number at any cross-section. Once the static

properties and area are known at a certain location, a simple derivation of $\dot{m} = \rho A V$ and a transformation of velocity to Mach number gives

$$M = \dot{m} RT / pAa \tag{2}$$

where $a$ is the speed of sound, represented as $\sqrt{(\gamma RT)}$ for a perfect gas, and $A$ is the flow cross-sectional area at the pressure-transducer location.

Mach number can also be found using pressure relationships from isentropic flow properties. If both total and static pressure are known at a certain location, then Mach number can be calculated. This is especially helpful in calculating Mach number at the exit plane of a supersonic nozzle[6]:

$$M = \sqrt{[2/(\gamma - 1)]\left[(p_0/p)^{(\gamma-1)/\gamma} - 1\right]} \tag{3}$$

## Results

### Pressure-Reading Analysis

The reservoir pressure shown in Fig. 12 and the vacuum-supply pressure, otherwise known as the backpressure, shown in Fig. 13 dictated the diffuser performance during test runs. Although the data in Figs. 12 and 13 are for a particular run, the same trends and general characteristics shown in these two figures were indicative for all test runs. Though not shown, both Figs. 12 and 13 have uncertainty bands of ±2 kPa (±0.3 psi) with a 95% confidence level.[5]

The initial dip in Figs. 12 and 13 indicates the vacuum butterfly valve opening. After the vacuum was allowed to pull on the test section for approximately 1 s, the compressed air was released into the test section. This is shown by the rapid increase in pressure at approximately the 2-s point. After the increase, the stilling chamber stabilized its reservoir pressure and settled into a steady state until the compressed air was switched off and the butterfly valve closed at approximately 28 s. For the particular plot shown in Fig. 12, the reservoir pressure reached a steady and consistent reading of about 183 kPa (26.5 psia) during the test run.

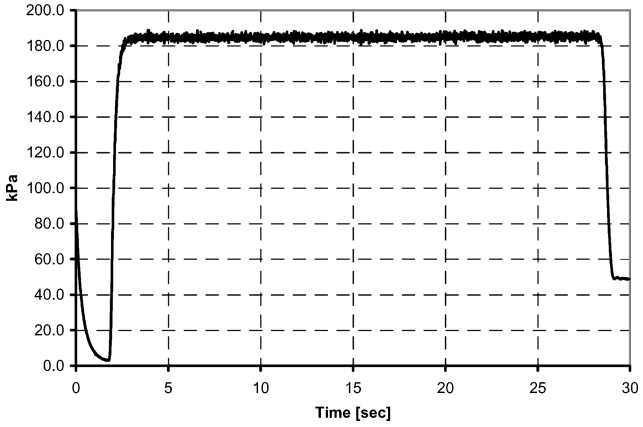


**Fig. 12 Typical reservoir pressure.**

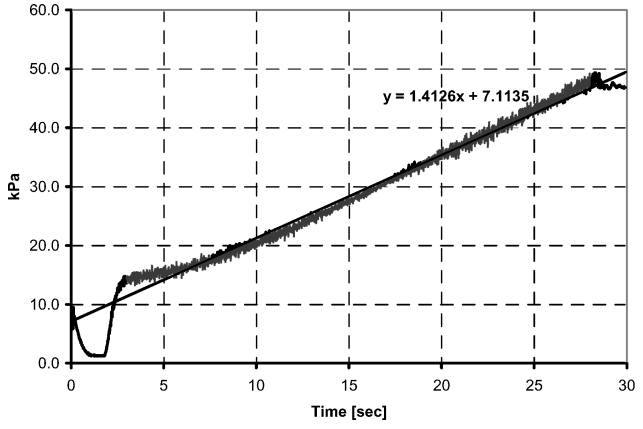


**Fig. 13 Typical backpressure.**

Figure 13 provides information on the nature of the lines connecting the test apparatus to the vacuum tank. The vacuum-supply pressure leveled at approximately 1.2 kPa (0.17 psia) after the butterfly valve was opened. As the compressed air entered the test section, the backpressure jumped to 13.8 kPa (2 psia). The jump in backpressure as the compressed air was released can be attributed to head loss within the vacuum system. The head loss was analytically determined to be 7.4 kPa (1.1 psia) and assumes an average velocity and density within the vacuum lines. While the compressed airflowed into the stilling chamber (reservoir) and through the nozzles at a constant reservoir pressure, the backpressure increased in a near-linear fashion. The linear regression line fit seen in Fig. 13 shows the backpressure rising at a rate of 1413 Pa/s (0.2 psi/s). Analytically, the backpressure was predicted to rise at a rate of 1759 Pa/s (0.26 psi/s). The rate at which the backpressure rises is dependent on the reservoir pressure. The higher the reservoir pressure, the higher the mass-flow rate, which causes a higher rate of change.

The mass-flow rate was calculated with Eq. (1). This calculation was applied at the throat of the nozzle, where the flow was assumed to be choked and the Mach number equal to one. For this particular test run, the mass flow was constant at a rate of 0.48 kg/s. The maximum error for a single mass-flow-rate calculation was determined to be ±4.7 g/s.[5]

The Mach number was calculated at PT1, PT2, and PT3 using Eq. (2) and the static-pressure measurement and cross-sectional area at each PT. The results are displayed in Fig. 14. The maximum error of a single Mach number calculation was ±0.1 (Ref. 5). The highest quasi-steady Mach number is shown to be at PT1, which was immediately downstream of the nozzle exit plane. The Mach number of the air is shown to decrease along the length of the diffuser. This is seen in the differences between PT1 and PT2. At PT1, the Mach number peaks and then levels at 2.7. Although Fig. 14 shows a peak above 2.7, the Mach number peak value is probably inaccurate. The inaccuracy is most likely due to the method used in calculating Mach number. The Mach numbers calculated in Fig. 14 are based on pressure measurements at each PT and the mass-flow rate at the nozzles. The calculations, once the compressed air is turned on, assume steady flow and that the mass flow rate is constant along the entire test section. In reality, however, transient conditions prevail in that early time interval as the flow is adjusting to reach a quasi-steady state. Initially, as the compressed air is introduced, the pressure readings are very low at the transducers and the mass-flow rate is high in the reservoir. Equation (2) shows that a high mass-flow rate combined with a low pressure will result in a higher-than-expected Mach number.

Once the pressure stabilizes, the flow downstream of the nozzles reaches quasi-steady state and a relatively constant Mach number, as shown in Fig. 14. The Mach number at PT2 levels at approximately 1.7, whereas the Mach number at PT3 levels at approximately 1.5. The decrease in Mach number from PT1 to PT2 is caused by an

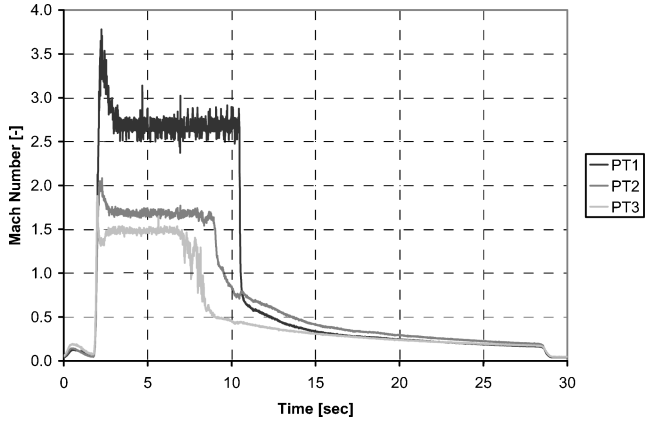


**Fig. 14 Mach numbers at PT1, PT2, and PT3.**

oblique shock formed at the leading edge of the centerbody. PT1 is in front of the shock, whereas PT2 is behind it. Mach number decreases across the shock, as shown in Fig. 14. This will be explained further in detail when the schlieren results are reported. The Mach number remains at this level until the flow at each location becomes subsonic due to the rising backpressure. Because PT3 is the closest out of the three transducers to the vacuum tank, the rising backpressure causes it to be the first transducer to record subsonic speeds. This is shown in Fig. 14 at approximately 7 s. PT2 follows at about 9 s, and finally PT1 records subsonic speeds at about 11 s. Because the compressed air was released into the reservoir at about 2 s, PT1 holds its steady state for approximately 9 s.

The Mach number at PT1 was also calculated by using Eq. (3). The two calculations matched to within 10% during the steady-state portion of the run. This gave a good indication that the cross-sectional area and temperature used in Eq. (2) were accurate.

**Schlieren Image Analysis**

The schlieren optical system was used to capture video and still images. After the compressed air is released into the reservoir, an oblique shock wave immediately forms off the leading edge of the centerbody, as shown at $t = 0.1$ s in Fig. 15.

This shock wave holds until approximately 7 s after the compressed air release. At this point, the backpressure has caused the shock wave to start moving towards the nozzle array. This process continues until the shock wave detaches from the leading edge and becomes perpendicular to the radial flow at $t = 10.25$ s. This gives a total test run time of over 10 s. In previous results with the unmodified transition structure, the oblique shock wave remained attached to the leading edge of the centerbody for only about 0.2 s.[5,6] This run-time extension is mostly due to the remodeling of the transition structure.

The measured shock wave angle at $t = 5.0$ s and the wedge half-angle dictate that the flow at the leading edge of the centerbody was traveling at a Mach number of approximately 2.8. Because the nozzle exit-plane Mach number was designed to be 2.2, the multiple jets must be underexpanded at the exit, and further expansion occurs after the nozzle exit plane to accelerate the fluid to Mach 2.8 at the leading edge of the centerbody.

As shown in Fig. 15, the shock becomes normal to the flow and detaches from the leading edge at $t = 10.25$ s. Figure 16 provides a sequence of images immediately following the ones shown in Fig. 15. The normal shock travels upstream toward the nozzles after detaching from the leading edge. At 15 s, it has almost reached the nozzle exit. At 20 s, multiple shock waves form to rapidly slow down the flow in order to meet the rising backpressure behind the shocks. Last, at 25 s, the waves move closer together and stand immediately downstream of the nozzle exit plane. The images in both Figs. 15 and 16 show that the flow is symmetric and radial.

The distance the lines are observed downstream of the nozzles can indicate whether the flow is underexpanded or overexpanded. Immediately after the compressed air is released into the test section, the nozzles are underexpanded. This is shown by the light curved lines downstream of the nozzles in Fig. 15 which indicate that the flow is still expanding. At $t = 25$ s in Fig. 16, the backpressure has driven the normal shock wave almost completely to the nozzle exit. For an overexpanded nozzle, the shock diamond pattern should extend no more than five to six nozzle widths from the exit plane.[7] Because the shock is within this range, it can be assumed that the nozzles become overexpanded at approximately 25 s. Therefore, for each test run, the nozzles start underexpanded until the backpressure rises high enough to drive the shock forward and make the nozzles overexpanded at approximately 25 s.

The amount of time for the nozzles to switch from underexpanded to overexpanded is dependent on the operating pressure in the stilling chamber (reservoir). A higher reservoir pressure produces a higher mass-flow rate, which will cause the backpressure to rise at a higher rate. The faster the backpressure rises, the faster the normal shock wave moves toward the nozzle exit plane. Therefore, the higher the reservoir pressure is, the faster the nozzles will become overexpanded.

Schlieren photographs were also taken immediately downstream of area 1 to get the full picture of the shock activity throughout the diffuser. These images can be seen in Fig. 17. As in area 1, an oblique shock is seen immediately after startup. The reflection of the oblique shock is seen off the outer wall. Because the shock appears to travel all of the way to the wall, this is an indication that there is no separated flow along the outer wall. The shock and reflections hold until approximately 6 s, where the shock wave starts to move forward. This is slightly ahead of the time at which the oblique shock wave attached to the centerbody moved forward in area 1. This is to be expected, because area 2 is farther downstream and closer to the diffuser exit. At $t = 10.25$ s, the shock waves are completely upstream, and the flow in area 2 is completely subsonic.

Another advantage to the view in area 2 is the picture of the second shock wave attached to the centerbody. In Fig. 15, it is barely seen at

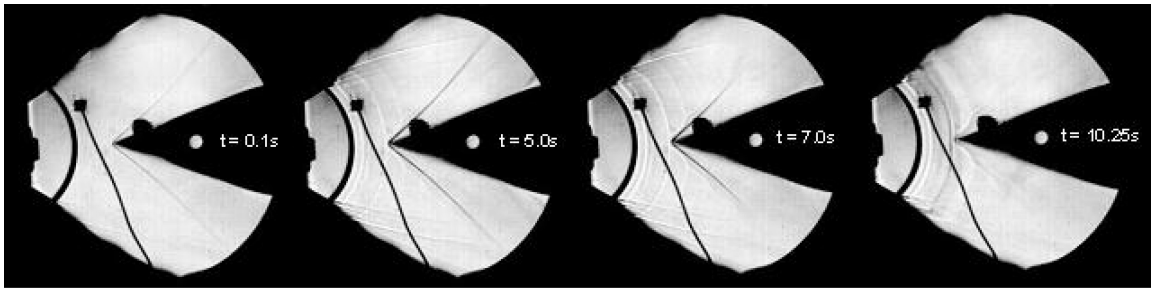


**Fig. 15 Schlieren images of oblique shock-wave motion in area 1.**

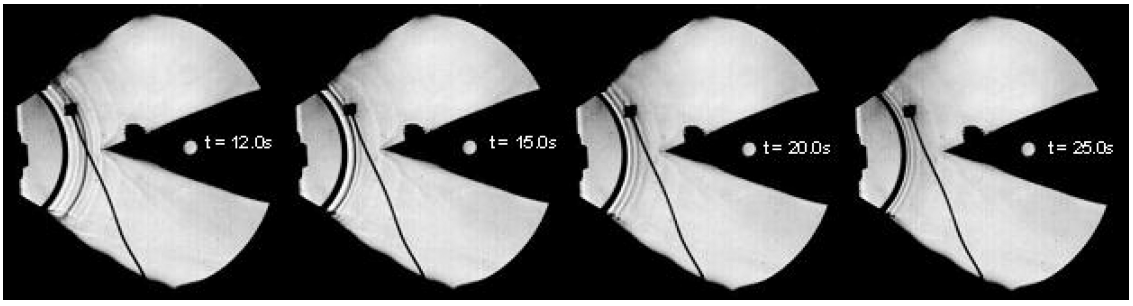


**Fig. 16 Schlieren images of normal shock-wave motion in area 1.**

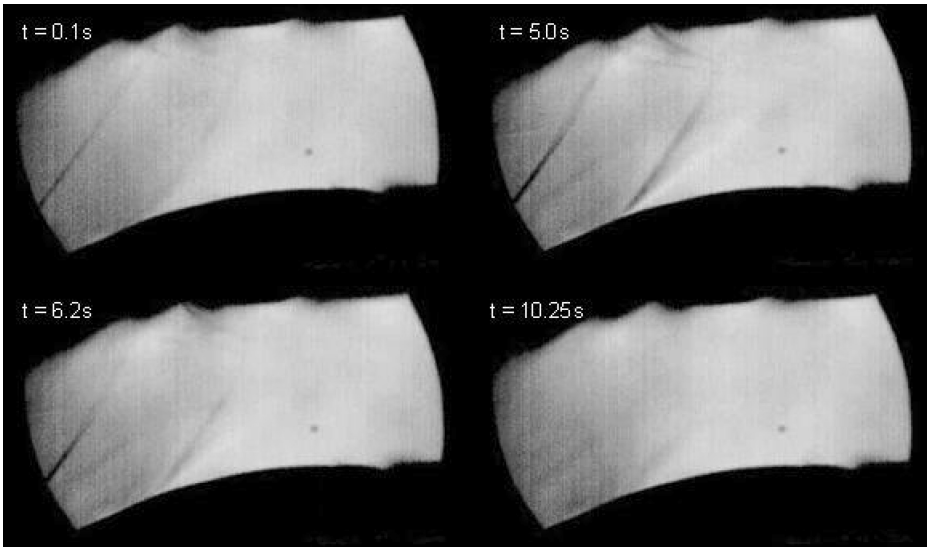


**Fig. 17 Schlieren images of oblique shock-wave motion in area 2.**

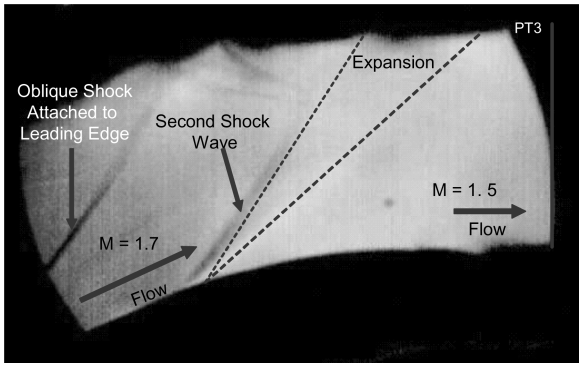


**Fig. 18 Detailed schlieren image of area 2 at time = 5.0 s.**

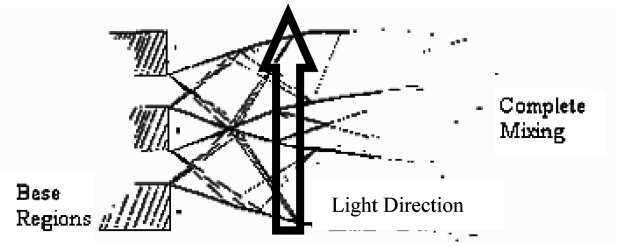


**Fig. 19 Schlieren light-source orientation.**

the far right side at $t = 5.0$ s. In Fig. 17 it is well defined and seen in its entirety. PT2 shows that during the steady-state period, the Mach number behind the shock is approximately 1.7. During the same time, Fig. 14 indicates that the Mach number at PT3 is approximately 1.5. This is shown in Fig. 18. After the flow passes the first oblique shock wave, it must turn 21 deg to become straight and flow along the midsection of the centerbody. According to expansion-wave theory, a flow at Mach 1.7 and turning 21 deg should accelerate to Mach 2.5 after the turn. However, Fig. 14 shows the flow at only Mach 1.5. This was measured at the location shown for PT3. Because the backpressure is constantly rising during the test run, flow at PT3 does not exceed Mach 1.5. This is the reason for the second shock wave indicated as shown in Fig. 18.

Flow must expand around a corner and, in turn, accelerate, according to theory. However, for the flow to accelerate to 1.5, the original flow before turning must be approximately 1.1. Therefore, an oblique shock wave must form before the turn to decelerate the flow after the initial shock from Mach 1.7 to 1.1. The flow then expands around the corner, as shown in Fig. 18, and accelerates to the measured Mach 1.5 at PT3. Therefore, it is evident that the flow conditions downstream dictate the activity upstream rather than the other way around.

The expansion of flow from the nozzle exit plane to the leading edge can be seen in the faint radial lines in the cavity normal to the flow seen in Fig. 15 at $t = 5.0$ s. These are most likely the intersecting expansion waves from each individual jet. Because of the orientation of the light source and the nozzle array, expansion and shock diamonds cannot be seen in the schlieren images. A diagram of the light source orientation through the nozzle exit plane can be seen in Fig. 19. The intersecting expansion and compression waves are the largest gradients in the image and appear as lines perpendicular to the flow as seen in Figs. 15 and 16. The light lines indicate expansion, whereas the dark ones show compression shocks.

**Comparison to CFD Results**

Comparing the experimental results to the CFD results obtained by TRW was part of the second objective of this research. Figure 20 displays a combined image of areas 1 and 2 at $t = 5.0$ s alongside a Mach line contour plot obtained numerically by TRW.[2]

The first thing to notice is that both results contain an oblique shock wave that forms off the leading edge of the centerbody. However, the angle for the shock wave in the CFD results is slightly higher. This results in a smaller Mach number of approximately 2.3 at the leading edge for the numerical results. As mentioned earlier, the angle for the experimental results indicates a Mach number of approximately 2.8 at the leading edge of the centerbody. This difference is probably due to the slight variations in geometry between the numerical and experimental subscale model. For instance, the scaled distance of the centerbody from the nozzle exit plane should be 1.2 according to the conceptual TRW design. However, the actual distance in the subscale mode is approximately 1.32 in. The larger distance may allow the flow to expand more before reaching the leading edge of the centerbody, which could explain the higher Mach number for the subscale model.

Another difference is that the experimental shock wave bends toward the nozzles as it gets closer to the outer wall, whereas the numerical shock wave bends toward the diffuser exit. This can attributed to the rising backpressure of the experimental results. In the numerical results shown below, a constant backpressure of 7 torr (0.15 psi) was used. For the experimental tests, the vacuum was able to evacuate the air in the test section down to approximately 3 torr (0.06 psi). However, after the compressed air was released into the system, the head loss jumped the pressure up to 13.8 kPa (2 psi) within approximately 0.1 s. Therefore, the rising backpressure for

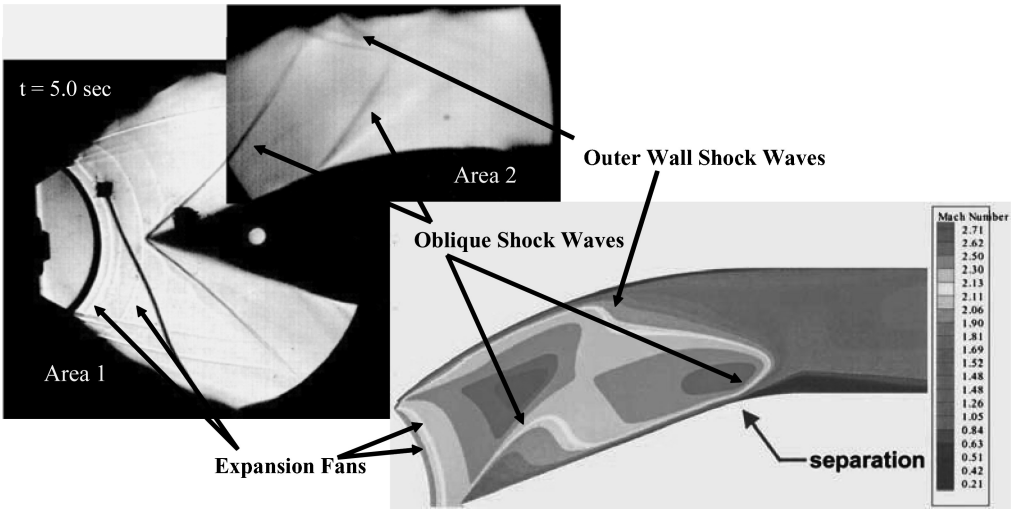


**Fig. 20 Comparison of experimental and CFD[2] results in areas 1 and 2.**

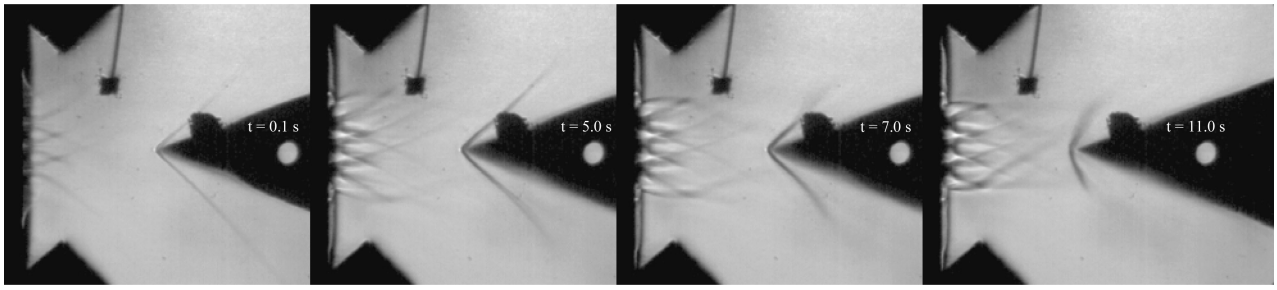


**Fig. 21 Straight nozzle flow in area 1.**

the experiment started out much higher than the constant backpressure for the numerical results. Because the backpressure was much less for the numerical results, and was constant throughout the test run, the shock wave was able to bend toward the diffuser exit rather than toward the nozzle array.

A second oblique shock wave is also seen in both results. Both of these shock waves occur where the centerbody turns to become straight and parallel with the outer wall. The difference between the two shock waves, however, is that an expansion fan occurs immediately after the experimental shock wave, while separation occurs behind the numerical shock wave. No evidence of separation is seen in the experimental results. The Mach number behind the second oblique shock wave matches the Mach number of the experimental results. Both show a Mach number of approximately 1.5 in this region.

Other points of interest between the two results are the curved expansion lines seen in both results. During the steady-state portion of the run, curved expansion lines are present in the region just downstream of the nozzles and up to the leading edge of the centerbody for both results as identified in Fig. 20. Because the cross-sectional area is increasing between the nozzle exit plane and the leading edge of the centerbody, the supersonic flow expands as it exits the nozzle array. This is similar for both results.

Finally, both results show shock waves coming off the outer walls as identified in Fig. 20. These waves are caused by reflections of the oblique shock wave attached to the leading edge of the centerbody and the outer wall straightening the flow. The shock waves from the experimental results start farther downstream than the ones shown in the CFD results.[2,3] This is due to the higher Mach number at the leading edge for the experimental tests. Because the Mach number at the leading edge is higher for the experimental tests, the shock wave coming off the leading edge has a smaller angle. This will cause the reflection off the outer wall from this wave to occur farther downstream.

Most of the differences between the two results can be attributed to the rising backpressure during experimental testing and slight differences in geometry between the numerical and subscale model. Despite these small differences, the images shown in Fig. 20 indicate that the two flows are very similar.

### Straight Nozzle Analysis

Flow and wave interactions from each straight nozzle were made visible because the nozzles were rotated 90 deg to the curved nozzles. Furthermore, the nozzle arrangement was planar rather than curved. Figure 21 shows a time sequence of the flow exiting the straight nozzles into area 1. The reservoir pressure for these test runs was matched to within 0.3 psi of that with the curved nozzle tests. This ensured that the pressure ratio across the nozzles was the same for both tests. Immediately after the compressed air was released, an oblique shock wave similar to that in Fig. 15 attached to the leading edge of the centerbody. With use of the angles of the wedge and the shock wave, the Mach number was calculated to be approximately 2.8 at the leading edge. This is identical to the Mach number calculated from Fig. 15 at $t = 5.0$ s.

The flow followed a pattern similar to that of Fig. 15. Initially, the nozzles were underexpanded at the nozzle exit plane and an oblique shock wave attached to the leading edge of the centerbody. During the steady-state portion of the test run, the oblique shock wave held its form and the individual jets of the nozzle array were fully interacting with each other. Notice how the oblique shock wave bowed forward toward the nozzle array as it got closer to the outer wall. This is similar to that in Fig. 15. At approximately 7 s, the backpressure caused the shock wave to move toward the leading edge of the centerbody. At approximately 11 s, the oblique shock wave was nearly detached from the leading edge. The shock wave was totally detached from the leading edge at approximately 13 s.

These actions and the times of their occurrence are slightly longer than those shown in Fig. 15. This can be attributed to the differing

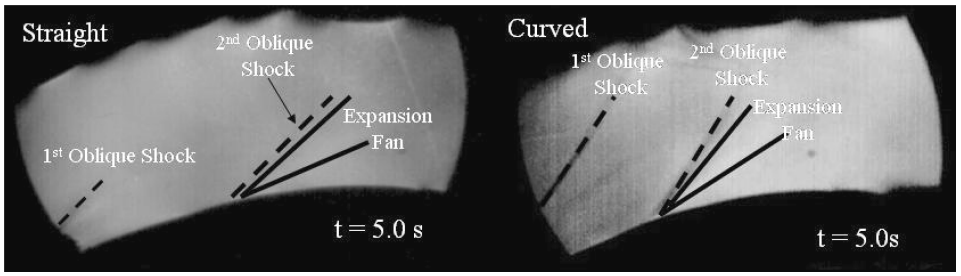


**Fig. 22 Shock activity in area 2 at $t = 5.0$ s.**

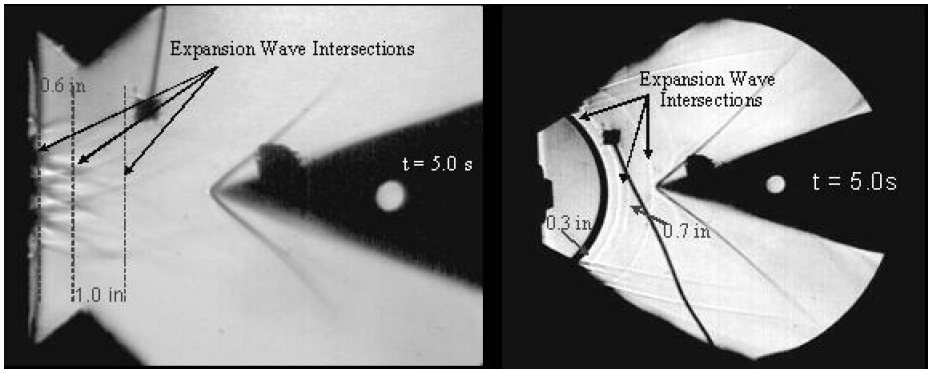


**Fig. 23 Expansion-wave intersections in optical cavity at $t = 5.0$ s.**

mass flows between the two tests. With the curved array, the 10 nozzles have a cross-sectional area of approximately 11 $cm^2$ at the throats. The straight nozzle array with a shorter length only has a total throat area of 5.27 $cm^2$. Because the straight array has almost half the area of the curved array, the mass flow rate is reduced by nearly half. During the steady-state period for both tests, the mass flow rates for the straight and curved arrays were 0.23 and 0.48 kg/s, respectively. Because the mass flow rate is less with the straight array, it takes longer for the vacuum tank to fill, and the backpressure does not rise as quickly. Therefore, it takes longer for the backpressure to cause subsonic flow upstream for the straight nozzle array.

Figure 21 also shows how the flow at the nozzle exit changes with time. At $t = 0.1$ and 5 s, it can be seen that the nozzles are underexpanded, because the flow expands outward toward the outer walls. As time progresses, the plumes become smaller and the flow does not expand outward as far. This is seen at $t = 7$ s. At $t = 11$ s, the flow exits the nozzles in an almost straight line. This confirms that the nozzles are underexpanded after startup, but transition to overexpanded as the backpressure rises.

The shock activity in area 2 is very similar for both the curved and straight nozzle arrays. Figure 22 identifies oblique shock waves and expansion fans for both nozzle arrays in area 2 during the steady state portion of each test run. The second oblique shock wave seems to occur at approximately the same location and the expansion wave occurs immediately downstream of the shock wave for both arrays. This gives a good indication that the two nozzle configurations provide similar flow conditions around the centerbody.

The schlieren images from Figs. 15 and 21 at $t = 5.0$ s are shown together in Fig. 23 to compare the steady-state images of the wave phenomena obtained with the straight (planar) nozzles (90 deg rotated) and with the curved nozzles with the same schlieren light-path direction. Figure 23 identifies expansion-wave intersections in the cavity region downstream of each of the nozzle arrays. The approximate distances between intersections are also shown. The flow seen in the first image of Fig. 23 compares with the underexpanded nozzle cluster drawing shown in Fig. 19. The first intersections seen are immediately after the nozzle exit plane. This is barely seen in the curved array image. Two more wave intersections can be seen downstream of the nozzle exit plane before reaching the leading edge of the centerbody. In the straight nozzle array, the second intersection occurs approximately 0.6 in. downstream of the nozzle exit, whereas

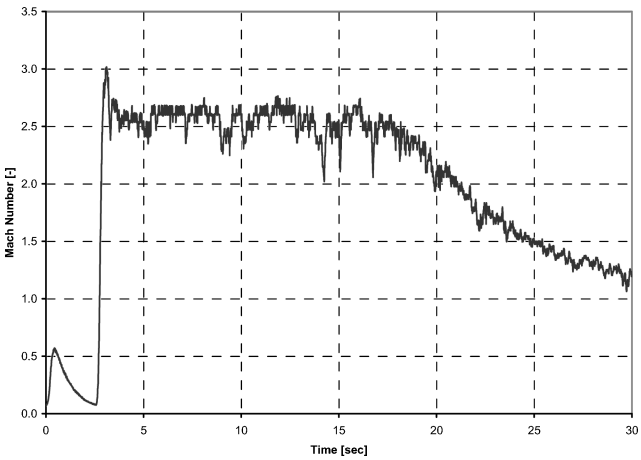


**Fig. 24 Mach number at PT6.**

the curved array shows a distance of approximately 0.3 in. The third intersection is almost 1 in. downstream of the second intersection for the straight array compared to 0.7 in. for the curved array. The distances for the straight nozzle array are approximately double the distances for the curved nozzle array. This can be attributed to the fact that the cross-sectional dimensions of the straight nozzles are twice the size of those in the curved array.

PT6 pressure data were collected approximately 0.25 in. downstream of the straight nozzle exit plane. The data were used to determine Mach number at this location. Figure 24 displays the Mach number at PT6.

The Mach number at PT6 shows a steady state from approximately 3 to 15 s. During this time the Mach number is approximately 2.7. Because the nozzles are designed for a Mach number of 2.2, expansion must occur immediately after the nozzle exit plane to increase the Mach number before PT6. This is confirmed by the first image in Fig. 23. The Mach numbers recorded by PT6 are nearly identical to the ones recorded by PT1 in the curved nozzle array. This further indicates that the flow conditions just downstream of the nozzle exit plane in the two different arrays are somewhat similar.

## Conclusions

The first objective was to remodel the previous test facility's transition section so that it would increase run time and be capable of investigating flow conditions in a simulated laser nozzle assembly and lasing cavity with use of cold flow. The transition section was remodeled to capture more area of the vacuum line entrance. The length of time the oblique shock wave remained attached to the leading edge increased dramatically from previous results. The transient interval time jumped from 0.2 s to approximately 10 s for an increase of roughly two orders of magnitude.

The second objective of this research was to examine the flow properties of the scaled nozzle/diffuser system. The experimental data collected from this facility could then be compared to the numerical results from TRW. Many similarities were noticed between the captured schlieren images and the results from TRW's CFD analysis. Most of the differences between the two results could be attributed to the rising backpressure during experimental testing and slight differences in geometry between the numerical and subscale model. Despite these small differences, the results indicate that the two flows are very similar. This subscale test facility can now be used to test models with different geometries related to a full-scale SBL exhaust system design.

## Acknowledgments

The authors thank Capt. Matthew E. Zuber for his superior guidance and encouragement throughout the course of this research. He provided keen insight and numerous recommendations to ensure our success and that of the U.S. Air Force. The views expressed herein are those of the authors and do not reflect the official policy or position of the U.S. Air Force, the Department of Defense, or the U.S. government.

## References

[1]Federation of American Scientists, "Space Based Laser (SBL)," Military Space Programs, 2002, URL: www.fas.org.

[2]Bautista, I., "Cold-Flow Testing of a Subscale Model Exhaust System for a Space-Based Laser," M.S. Thesis, AFIT/GAE/ENY/03-1, Air Force Inst. of Technology, Wright–Patterson AFB, OH, March 2003.

[3]Bautista, I. S., and Franke, M. E., "Cold-Flow Testing of a Subscale Model Exhaust System for a Space-Based Laser," AIAA Paper 2003-3754, June 2003.

[4]Perram, G. P., "Chemical Lasers," *Encyclopedia of Physical Science and Technology*, 3rd ed., Vol. 8, Academic Press, New York, 2001, pp. 283–295.

[5]Bergren, S., "Fabrication and Cold-Flow Testing of Subscale Space-Based Laser Geometry," M.S. Thesis, AFIT/GAE/ENY/02-3, Air Force Inst. of Technology, Wright–Patterson AFB, OH, March 2002.

[6]Bergren, S. E., and Franke, M. E., "Fabrication and Cold Flow Test of a Model of Nozzle Rings and Exhaust Manifold," AIAA Paper 2002-2129, May 2002.

[7]Anderson, J. D., *Modern Compressible Flow*, 3rd ed., McGraw–Hill, New York, 2003, Chap. 5.

I. Boyd
*Associate Editor*